

# Shadow Area and Degrees-of-Freedom for Free-Space Communication

Mats Gustafsson

**Abstract**—The number of degrees-of-freedom (NDoF) in a communication system is limited by the number of antenna ports, element shapes, positions, and the propagation environment. As the number of antenna elements increases within a given region, the NDoF eventually saturates due to correlation of the radiated fields. The maximal NDoF can be determined numerically for communication between two regions using singular value decomposition of a channel model representing wave propagation between densely sampled sources at the transmitter and fields at the receiver. This paper provides a straightforward analytical estimate of the NDoF for arbitrarily shaped transmitter and receiver regions. The analysis shows that the NDoF for electrically large regions is approximated by the mutual shadow area of the regions, measured in wavelengths. Several setups illustrate the results, which are then compared with numerical evaluations of the singular values of the propagation channel. These new analytical expressions also simplify to previously established results based on Weyl’s law and the paraxial approximation.

**Index Terms**—Degrees of freedom, capacity, antenna theory, electromagnetic theory, modes

## I. INTRODUCTION

Electromagnetic degrees-of-freedom (DoF) are critical parameters in communication systems, providing a fundamental estimate of the system’s potential performance [1]–[8]. The number of degrees-of-freedom (NDoF) is particularly significant, as the capacity of a communication system tends to increase approximately linearly with the NDoF. This relationship underscores the importance of accurately determining and maximizing the NDoF in the design and analysis of advanced communication systems.

In the context of wave-based communication, DoF encompasses various components, including temporal, spatial, and polarization aspects. Each of these components contributes to the overall capacity and efficiency of the communication system [5]. The concept of NDoF extends beyond communication systems and plays a crucial role in fields such as imaging, radar, and antennas. Early investigations by Di Francia in the mid-20th century highlighted the significance of NDoF in these areas [9], [10]. For instance, in imaging, NDoF determines the resolution and quality of the reconstructed images [11], [12].

Wave propagation in canonical geometries, such as spherical symmetric setups or rectangular waveguides, has traditionally been used to determine the NDoF for both electromagnetic

and scalar fields [11]–[15]. These findings can be interpreted as specific manifestations of Weyl’s law [16], [17], formulated in the early twentieth century by Hermann Weyl. Weyl’s law describes the asymptotic eigenvalue distributions of Laplace and Helmholtz equations in bounded regions, demonstrating that the number of propagating waves, and hence NDoF, is proportional to the region’s size, measured in wavelengths [18].

These estimates are instrumental in determining the NDoF in arbitrarily shaped waveguides and for radiation emanating from convex-shaped regions. Additionally, Landau’s eigenvalue problem offers a framework for analyzing NDoF [5]. Numerical techniques, such as singular value decompositions (SVD) combined with free-space propagation models utilizing Green’s function (dyadic), further enable the determination of NDoF for regions of arbitrary shapes [19]–[22]. In recent years, extensive research has focused on future communication systems, necessitating a deeper understanding of wave propagation and NDoF in complex environments [1], [2], [23]–[27].

This paper aims to bridge analytical and numerical approaches to provide insights into the NDoF between arbitrarily shaped transmitter and receiver regions, NDoF between arbitrarily shaped transmitter and receiver regions, thereby providing a comprehensive framework for assessing and enhancing the performance of modern communication and sensing systems. This paper provides an analytical estimate of the NDoF for free-space communication between arbitrarily shaped transmitter and receiver regions. The results suggest that the mutual shadow area of these regions, measured in wavelengths, accurately estimates the NDoF for sufficient short wavelengths. The mutual shadow area is easily evaluated for various configurations, offering valuable physical insight and understanding. These new analytical expressions also include previously established results based on Weyl’s law, shadow area [18], and the paraxial approximation [20].

Numerical evaluations of the singular values of the propagation channel for several setups are used to illustrate the results. It is demonstrated that the singular values primarily depend on the NDoF, and plotting normalized singular values for different setups with the same NDoF reveals a tendency of the singular values to cluster for large NDoF. To address the computational challenge of evaluating singular values of the channel matrix as the electrical size increases, a randomized SVD algorithm exploiting the low-rank structure is employed [28].

The setup and free-space communication channel are presented in Sec. II. The NDoF and shadow area for a circumscribing receiver structure are discussed in Sec. III, followed by a proposed generalization to a partly circumscribing structure in Sec. IV. Communication between volumes and mutual shadow area is introduced in Sec. V. Secs. VI and VII present

Manuscript received August 1, 2024; revised August 1, 2024. This work was supported by ELLIIT - an Excellence Center at Linköping-Lund in Information Technology and the TICRA foundation.

M. Gustafsson is with Lund University, Lund, Sweden, (e-mails: mats.gustafsson@eit.lth.se).

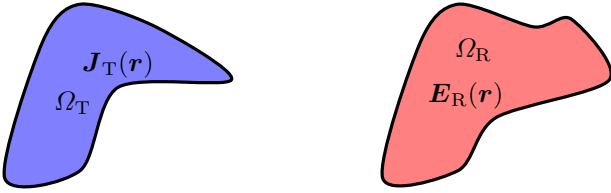


Figure 1. Communication channel between a transmitting region  $\Omega_T$  and receiving region  $\Omega_R$ , represented by the radiated field  $\mathbf{E}_R$  in  $\Omega_R$  generated by current densities  $\mathbf{J}_T$  in  $\Omega_T$ .

numerical results in 2D and 3D, respectively. The paper is concluded in Sec. VIII.

## II. FREE-SPACE COMMUNICATION CHANNEL

Communication between antenna systems confined to a transmitting region  $\Omega_T$  and a receiving region  $\Omega_R$  can be modeled by the radiation from current densities  $\mathbf{J}_T(\mathbf{r})$  in  $\Omega_T$  to fields  $\mathbf{E}_R(\mathbf{r})$  in  $\Omega_R$ , as illustrated in Fig. 1. For simplicity, we consider transmitting electric currents  $\mathbf{J}_T$  and receiving electric fields  $\mathbf{E}_R$ , but the results and model are also applicable to scenarios involving both electric and magnetic currents, as well as electric and magnetic fields.

The transfer of information from  $\Omega_T$  to  $\Omega_R$  depends on the number of independent temporal and spatial channels that can be formed between these regions. The number of temporal channels is proportional to the available bandwidth [29], [30] and is not strongly linked to the geometrical configuration of the regions for electrically large structures. Here, we focus on the spectral efficiency (capacity per unit bandwidth) [29], [30]. Spectral efficiency depends on the spatial channels between the regions and the signal-to-noise ratio (SNR).

The spectral efficiency, or capacity, is determined by Shannon's formula for a channel formed by antenna systems in  $\Omega_T$  and  $\Omega_R$  at a given SNR [29], [30]. This capacity increases with an improved SNR and by including more (ideal) antenna elements in the regions. The increase in capacity is nearly linear up to a certain number of elements and saturates beyond this point [5]. Increasing the number of elements after saturation requires a significantly higher SNR to further enhance the capacity. This threshold number of antenna elements (ports) is referred to as the number of degrees of freedom (NDoF) [5]. The NDoF depends on the geometrical configuration of  $\Omega_T$  and  $\Omega_R$  and the frequency  $f$  or wavelength  $\lambda = c/f$ , where  $c$  denotes the speed of light.

The NDoF between two regions is often determined from the channel formed by a transmitting array in  $\Omega_T$  and a receiving array in  $\Omega_R$ . These arrays are created by discretizing the regions into sub-wavelength spaced point or dipole elements [19], [20]. This approach is analogous to decomposing the current density into a set of basis functions, where each basis function corresponds to an array element [31]. Using  $N_T$  transmitting elements and  $N_R$  receiving elements defines a channel matrix  $\mathbf{H}$  with dimensions  $N_R \times N_T$ .

Forming an SVD of the channel matrix  $\mathbf{H}$  reveals a threshold number, after which the singular values decrease rapidly. The slope of this decay increases with increasing frequency

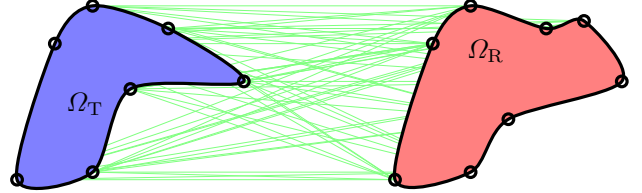


Figure 2. Communication channel represented as paths between transmitting and receiving array elements, here represented by 7 transmitters and 8 receivers indicated by the markers.

(decreasing wavelength). The effective NDoF is a way to approximate this threshold and the NDoF as [25], [32]

$$N_e = \frac{\|\mathbf{H}\|_F^4}{\|\mathbf{H}\mathbf{H}^H\|_F^2} = \frac{(\sum_n \sigma_n)^2}{\sum_n \sigma_n^2}, \quad (1)$$

where  $\sigma_n$  denotes the squared singular values of  $\mathbf{H}$ , *i.e.*, eigenvalues of the correlation matrix

$$\sigma_n = \text{eig}(\mathbf{H}\mathbf{H}^H), \quad (2)$$

the superscript  $H$  denotes Hermitian transpose, and  $\|\cdot\|_F$  is the Frobenius norm [33]. These approaches and approximations have been thoroughly investigated in the literature [25], [32]. The effective NDoF is easy to evaluate and useful for arbitrary configurations and wavelengths.

The effective NDoF and distribution of the singular values are independent of the normalization of the channel matrix  $\mathbf{H}$ . For the presentation in this paper, it is convenient to normalize the channel matrix with its Frobenius  $\|\mathbf{H}\|_F$ , *i.e.*,  $\tilde{\mathbf{H}} = \mathbf{H}/\|\mathbf{H}\|_F$ . This normalization is equivalent to normalizing the eigenvalues  $\sigma_n$  as

$$\zeta_n = \sigma_n / \sum_n \sigma_n \quad (3)$$

with  $\zeta_n$  denoting the eigenvalues of the normalized correlation matrix, *i.e.*,  $\zeta_n = \text{eig}(\tilde{\mathbf{H}}\tilde{\mathbf{H}}^H)$ . These normalized eigenvalues satisfy

$$\sum \zeta_n = 1 \quad \text{and} \quad \sum \zeta_n^2 = N_e^{-1}. \quad (4)$$

In this paper, we use simple geometrical properties of the regions  $\Omega_T$  and  $\Omega_R$  to estimate a NDoF,  $N_A$ , in the asymptotic limit  $\lambda \rightarrow 0$ . This estimate is compared with an ideal uniform channel having  $N_A$  non-zero eigenvalues, each with an amplitude of  $N_A^{-1}$ , as illustrated in Fig. 3. The ideal uniform channel has a sharp bend, often referred to as a *corner* or *knee*, at the point  $(1, 1)$ , when the eigenvalue index  $n$  and eigenvalues are normalized with  $N_A$ .

The eigenvalues of a non-ideal channel decay rapidly after the NDoF estimated by  $N_A$ , as shown for the channel between two square plates in Fig. 3 using  $N_A \in \{500, 1000\}$ , corresponding to  $\ell/\lambda \in \{28, 40\}$  wavelengths per side. This channel forms a corner with a finite curvature. The evaluation of  $N_A$  semi-analytically from the shadow of the geometrical structure and  $\zeta_n$  numerically from the channel, as shown in Fig. 2, is discussed in the remainder of this paper.

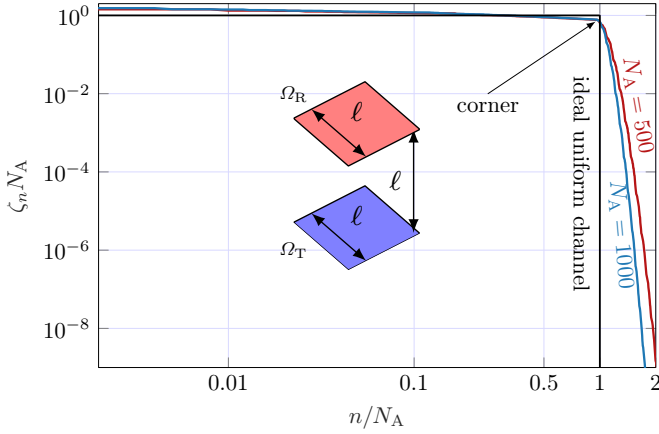


Figure 3. Distribution of the normalized eigenvalues,  $\zeta_n$ , in (3) for an ideal uniform channel compared with that of a free-space channel between two square regions, each with side length  $\ell$ , separated by a distance  $\ell$ , as depicted in the inset.

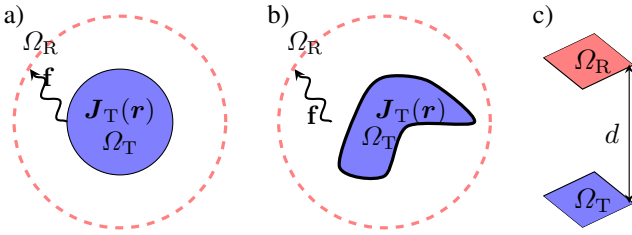


Figure 4. Free-space channel and DoF for: a) regions with spherical (cylindrical) symmetry, b) arbitrary shaped transmitter region  $\Omega_T$  circumscribed by a spherical (cylindrical) receiver region, c) two parallel regions separated a distance  $d$ .

### III. NDOF ESTIMATES AND SHADOW AREA

Analytic solutions of the wave equation or Maxwell's equations can be used to estimate the NDoF for canonical geometries, such as regions with spherical or cylindrical symmetries, by expanding the field in spherical and cylindrical waves, respectively [34], [35]. The NDoF for a spherical region with radius  $a$  surrounded by a larger spherical region, see Fig. 4a, has been investigated using various techniques [12], [13], [36]–[38]. These studies have found that electrically small regions, with  $ka \ll 1$ , exhibit six (polarization) DoF, while regions with  $ka \gg 1$  have  $(ka)^2$  DoF per polarization, where  $k = 2\pi/\lambda$  denotes the wavenumber. In the corresponding 2D case with circular (cylindrical) symmetry, the expansion in cylindrical waves yields approximately  $2ka$  DoF for  $ka \gg 1$ . When expressed in terms of surface area  $A$  and circumference  $L$ . The NDoF for cylindrical and spherical regions become  $2L/\lambda$  and  $\pi A/\lambda^2$ , respectively.

The spherical and circular geometries can be considered special cases of Weyl's law [18]. Weyl's law describes the asymptotic distributions of eigenvalues for the Laplace and Helmholtz operators in a region with Dirichlet or Neumann boundary conditions [16], [17]. For arbitrarily shaped waveguides, the number of propagating (scalar) modes is asymptotically given by Weyl's law [18]

$$N_W \approx \frac{2L}{\lambda} \quad \text{and} \quad N_W \approx \frac{\pi A}{\lambda^2} \quad (5)$$

for a line with length  $L$  and an aperture surface with area  $A$ , respectively.

Weyl's law estimates the NDoF for arbitrary convex-shaped regions  $\Omega_T$  circumscribed by a large spherical (cylindrical) receiving region  $\Omega_R$  [18]. The NDoF, as quantified by area and length in Weyl's law, can be interpreted in terms of sampling. Specifically, the density of independent transmitters on a line is  $\lambda/2$ , consistent with Nyquist sampling and array theory, while it is  $\lambda/\sqrt{\pi} \approx \lambda/1.8$  for a surface [1], [2]. However, the surface area  $A$  and length  $L$  in Weyl's law do not account for blockage for non-convex shapes.

The NDoF for non-convex transmitting regions  $\Omega_T$ , see Fig. 4b, is determined by investigating the ability of the transmitter to generate waves in directions  $\hat{k}$  or, by reciprocity, to receiving plane waves propagating in the opposite direction [18]. This concept leads to the notion of shadow area in the asymptotic limit  $\lambda \rightarrow 0$  [18], [37]. The shadow area of a region  $\Omega_T$  for a direction  $\hat{k}$  quantifies how transmitters confined to the region can direct radiation in that direction. For convex shapes, this reduces to the classical cross-sectional area, commonly used to estimate the effective area for aperture antennas [39].

An object circumscribed by a (convex) receiving region  $\Omega_R$  can interact with plane waves propagating in any direction, necessitating a summation over all directions. The total shadow area is formed by integrating the shadow area over a sphere (or circle for a line). The resulting NDoF for an arbitrarily shaped object surrounded by a large spherical region is approximately [18]

$$N_A = \frac{L_s}{\lambda} \quad \text{and} \quad N_A = \frac{A_s}{\lambda^2}, \quad (6)$$

where  $A_s$  denotes the total shadow area ( $L_s$  for length) of the object and  $\lambda$  is much smaller than the object's dimensions. These results reduce to Weyl's law for convex shapes, as the average shadow area is a quarter of the surface area  $\langle A_s \rangle = A/4$  [40], giving the total shadow area  $A_s = 4\pi \langle A_s \rangle = \pi A$ , consistent with Weyl's law (5). Similarly, in 2D  $L_s = 2\pi \langle L_s \rangle = 2L$ .

The total shadow area estimates the NDoF that can be transmitted from a region  $\Omega_T$  to the far field [18]. This provides a limit that is independent of the receiver location and configuration. For line-of-sight communication between well separated planar regions the paraxial approximation can be used [19], [20]. This asymptotic solution for narrow angular propagation provide closed form expressions for the NDoF for planar regions with areas  $A_T$  and  $A_R$  separated a distance  $d$ , see Fig. 4c, as [19], [20]

$$N_P = \frac{L_T L_R}{d\lambda} \quad \text{and} \quad N_P = \frac{A_T A_R}{d^2 \lambda^2} \quad (7)$$

(per polarization) with  $d$  much larger than the object sizes. The paraxial approximation can also be related to the shadow area (length), specifically the shadow area (length) of the transmitter cast on the receiver. For large distances and an infinitesimally small transmitter region, this length is given by  $\Delta L_T L_R/d$  and the area by  $\Delta A_T A_R/d^2$ . Summing over the transmitter yields (7).

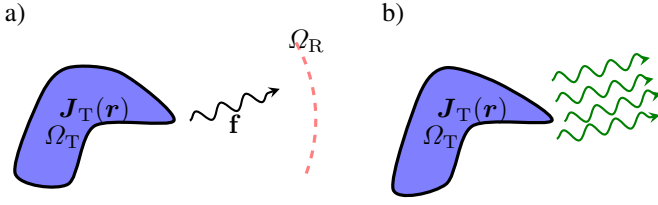


Figure 5. a) Communication from a transmitter in  $\Omega_T$  to a partly circumscribing region  $\Omega_R$ . b) Representation using rays propagating in directions  $\mathbf{k}$ .

#### IV. PARTLY CIRCUMSCRIBING STRUCTURE

NDofF for communication between transmitters in the region  $\Omega_T$  to receivers in the far field partly circumscribing the transmitter, or similarly, on a large partly circumscribing sphere  $\Omega_R$ , as shown in Fig. 5a is investigated first. It reduces to the case with circumscribing receivers (6) in one limit and the paraxial approximation (7) in the other. Current density  $\mathbf{J}_T(\mathbf{r})$  in the transmitting region  $\Omega_T$  constitutes sources for the radiated field and are expanded in sufficiently large number of basis functions, with expansion coefficients collected in a column matrix  $\mathbf{I}$  [31]. It is assumed that the transmitting region  $\Omega_T$  is constructed of some material with minimal material losses described by a loss matrix  $\mathbf{R}_\rho$  [18]. Similarly, the radiated field over the receiver region is obtained by integrating the field over  $\Omega_R$ . This integration is power normalized and involves a quadrature scheme with quadrature weights  $\Lambda_p^2$  for quadrature points (directions)  $\hat{\mathbf{k}}_p$  and polarizations  $\hat{\mathbf{e}}_p$  with  $p \in [1, N_R]$ . Here, we for simplicity assume that the quadrature weights are positive, negative weights such as in Lebedev quadrature can also be considered [41]. We use a spherical (or cylindrical) coordinate system with directions  $\hat{\mathbf{k}}_p$  described by polar  $\theta_p$  and azimuthal  $\phi_p$  coordinates and polarizations in the  $\hat{\theta}_p$  and  $\hat{\phi}_p$  directions [35]. The quadrature weights can also be interpreted as an SNR weight for a communication system, which also include point measures for receivers in discrete directions.

Collect the received field in a column matrix  $\mathbf{f} = \mathbf{\Lambda}\mathbf{F}\mathbf{I}$ , where  $\mathbf{F}$  is a matrix describing the linear map from the currents to the received field in the quadrature points  $\hat{\mathbf{k}}_p$  and polarizations  $\hat{\mathbf{e}}_p$  [41] including the square root of the quadrature weights collected in the diagonal matrix  $\mathbf{\Lambda}$ . The capacity (spectral efficiency) of this communication system  $\mathbf{f} = \mathbf{\Lambda}\mathbf{F}\mathbf{I} + \mathbf{n}$  constrained by  $\text{Tr}(\mathbf{R}_x\mathbf{P}) = 1$  is determined by [18], [42]

$$\begin{aligned} & \text{maximize} && \log_2(\det(\mathbf{1} + \gamma\mathbf{\Lambda}\mathbf{F}\mathbf{P}\mathbf{F}^H\mathbf{\Lambda})) \\ & \text{subject to} && \text{Tr}(\mathbf{R}_x\mathbf{P}) = 1 \\ & && \mathbf{P} \succeq \mathbf{0}, \end{aligned} \quad (8)$$

where  $\mathbf{P} = \mathcal{E}\{\mathbf{I}\mathbf{I}^H\}$  denotes the covariance matrix of the currents,  $\gamma$  quantifies the SNR from the additive noise  $\mathbf{n}$ , and  $\mathbf{1}$  denotes the identity matrix. In (8), the current is without loss of generality normalized to a fixed value. The power constraint  $\text{Tr}(\mathbf{R}_x\mathbf{P}) = 1$  with  $\mathbf{R}_x$  a symmetric positive definite matrix is used to model different communication situations. Considering *e.g.*, the dissipated power  $\frac{1}{2}\mathbf{I}\mathbf{R}\mathbf{I}$  in radiation and

material losses uses the method of moments (MoM) resistance matrix [31]  $\mathbf{R}_x = \mathbf{R}$ . The resistance matrix  $\mathbf{R}$  can be decomposed into its radiation  $\mathbf{R}_0$  and material part  $\mathbf{R}_\rho$  [31], [43], where  $\frac{1}{2}\mathbf{I}^H\mathbf{R}_0\mathbf{I}$  and  $\frac{1}{2}\mathbf{I}^H\mathbf{R}_\rho\mathbf{I}$  model radiated power and power dissipated in ohmic or dielectric losses. Constraining only material losses uses  $\mathbf{R}_x = \mathbf{R}_\rho$  in (8). These material losses can also be interpreted as a constraint on the amplitude of the current density for a region with homogeneous losses modelled by a resistivity  $\rho_r$  and the loss matrix  $\mathbf{R}_\rho = \rho_r\mathbf{\Psi}$  with the Gram matrix [33]  $\mathbf{\Psi}$  and least-squared norm of the current density  $\mathbf{I}^H\mathbf{\Psi}\mathbf{I}$ , see App. A. Alternative formulations of (8) include constraints on efficiency [42], [44] or bandwidth from the reactive energy around the antenna [44], [45].

The capacity (8) is determined by the water-filling algorithm [29] for which it is convenient to rewrite (8) by a change of variable  $\tilde{\mathbf{P}} = \mathbf{G}\mathbf{P}\mathbf{G}^H$ , where  $\mathbf{R}_x = \mathbf{G}^H\mathbf{G}$  is a factorization of a symmetric positive definite matrix [33]. Substituting  $\tilde{\mathbf{P}}$  into (8) results in

$$\begin{aligned} & \text{maximize} && \log_2(\det(\mathbf{1} + \gamma\mathbf{H}\tilde{\mathbf{P}}\mathbf{H}^H)) \\ & \text{subject to} && \text{Tr}(\tilde{\mathbf{P}}) = 1 \\ & && \tilde{\mathbf{P}} \succeq \mathbf{0} \end{aligned} \quad (9)$$

with the channel matrix  $\mathbf{H} = \mathbf{\Lambda}\mathbf{F}\mathbf{G}^{-1}$ . This optimization problem is diagonalized by an SVD of the channel matrix  $\mathbf{H}$ , *i.e.*, square roots of the eigenvalues of  $\mathbf{H}^H\mathbf{H} = \mathbf{G}^{-H}\mathbf{F}^H\mathbf{\Lambda}^2\mathbf{F}\mathbf{G}^{-1}$ , which can be written  $\mathbf{G}^{-H}\mathbf{F}^H\mathbf{\Lambda}^2\mathbf{F}\mathbf{G}^{-1}\mathbf{V}_n = \nu_n\mathbf{V}_n$ . Simplifying by multiplication with  $\mathbf{G}^H$  and setting  $\mathbf{I}_n = \mathbf{G}^{-1}\mathbf{V}_n$  results in the generalized eigenvalue problem

$$\mathbf{F}^H\mathbf{\Lambda}^2\mathbf{F}\mathbf{I}_n = \nu_n\mathbf{R}_x\mathbf{I}_n. \quad (10)$$

This eigenvalue problem reduces to radiation mode efficiency for a receiving structure circumscribing the transmitter [18], [42], [46], and here we for simplicity refer to the modes  $\mathbf{I}_n$  in (10) as generalized radiation modes. These modal currents are orthogonal over the resistance matrix  $\mathbf{R}_x$  and region  $\Omega_R$

$$\mathbf{I}_m^H\mathbf{R}_x\mathbf{I}_n = \delta_{mn} \quad \text{and} \quad \mathbf{f}_m^H\mathbf{f}_n = \mathbf{I}_m^H\mathbf{F}^H\mathbf{\Lambda}^2\mathbf{F}\mathbf{I}_n = \nu_n\delta_{mn}. \quad (11)$$

Generalized radiation modes (10) maximize the (Rayleigh) quotient between the radiated power over the directions  $\Omega_R$  and dissipated power quantified by  $\mathbf{R}_x$

$$\frac{\text{radiated power in } \Omega_R}{\text{dissipated power}} = \frac{\mathbf{I}_m^H\mathbf{F}^H\mathbf{\Lambda}^2\mathbf{F}\mathbf{I}_n}{\mathbf{I}_m^H\mathbf{R}_x\mathbf{I}_n} = \delta_{mn}\nu_n. \quad (12)$$

Using  $\mathbf{R}_x = \mathbf{R}$  interprets the eigenvalues  $\nu_n \in [0, 1]$  as an efficiency for orthogonal currents in  $\Omega_T$  where only radiation in the region  $\Omega_R$  is accounted for.

Geometry and material properties of  $\Omega_T$  and configuration of  $\Omega_R$  are contained in the generalized radiation modes (10). The generalized radiating modes diagonalizes (9) which solved using waterfilling [29] over radiation mode efficiencies  $\nu_n$  results in

$$\max_{\sum \tilde{P}_n = 1} \sum_{n=1}^N \log_2(1 + \gamma\nu_n\tilde{P}_n), \quad (13)$$

with a finite number of non-zero power levels  $\tilde{P}_n$  associated with radiation modes of sufficiently high efficiency. Water-filling algorithm solves (13) and distributes the power  $\tilde{P}_n$

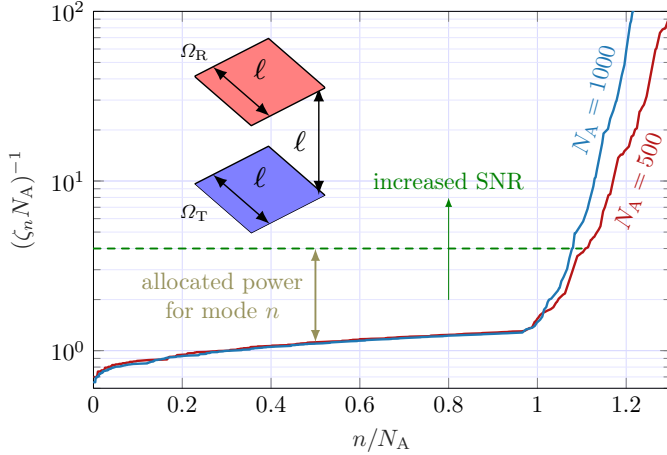


Figure 6. Reciprocal of the eigenvalues for the channel correlation matrix of two parallel squares with side length  $\ell$  separated a distance  $\ell$  using  $N_A \in \{500, 1000\}$ , cf., Fig. 3.

over the modes [29] analogous to filling a bucket with heights proportional to  $\nu_n^{-1}$  with water.

The reciprocal of the normalized eigenvalues  $(\zeta_n N_A)^{-1}$  are plotted in Fig. 6 for the channel between the two rectangles shown in Fig. 3. For a given SNR (power level), illustrated by the dashed line in Fig. 6 the allocated power is proportional to the distance down to  $(\zeta_n N_A)^{-1}$ . This illustrates the high cost in SNR to use more than  $N_A$  modes. The eigenvalues  $(\zeta_n N_A)^{-1}$ , related to the problem in (2) reduces to (2) for a matrix  $\mathbf{R}_x = \mathbf{R}_p$  that is proportional to the identity matrix. This occurs, e.g., in the case of homogeneous losses and a current density expanded in identical and orthogonal basis functions, or when uniformly sampled with point sources, see App. A.

Determination of the NDoF from the number of generalized radiation modes (10) is easily achieved numerically for arbitrary shaped objects, material parameters, and receiver configurations. Analytical solutions in the asymptotic limit  $\lambda \rightarrow 0$  complement the numerical results and provide physical insight and understanding.

An analytical solution is found by relating the sum of the eigenvalues  $\nu_n$  to geometrical properties of  $\Omega_T$  and  $\Omega_R$  obtained by the maximal effective area. The sum of the eigenvalues  $\nu_n$  is given by the trace [33]

$$\begin{aligned} \sum_{n=1}^N \nu_n &= \text{Tr}(\mathbf{G}^{-\text{H}} \mathbf{F}^{\text{H}} \mathbf{\Lambda}^2 \mathbf{F} \mathbf{G}^{-1}) = \text{Tr}(\mathbf{R}_x^{-1} \mathbf{F}^{\text{H}} \mathbf{\Lambda}^2 \mathbf{F}) \\ &= \text{Tr}(\mathbf{F} \mathbf{R}_x^{-1} \mathbf{F}^{\text{H}} \mathbf{\Lambda}^2) = \sum_{p=1}^{N_p} \Lambda_p^2 \mathbf{F}_p \mathbf{R}_x^{-1} \mathbf{F}_p^{\text{H}}, \end{aligned} \quad (14)$$

where cyclic permutations of the trace operator  $\text{Tr}$  are used and  $\mathbf{F}_p$  denotes row  $p$  of  $\mathbf{F}$ .

The identity (14) is valid for arbitrary constraints  $\mathbf{R}_x$  in (8). Here, we consider  $\mathbf{R}_x = \mathbf{R}$  to constrain the dissipated power (radiation and losses) and  $\mathbf{R}_x = \mathbf{R}_p$  to constrain material losses (or equivalently the norm of the current density). For the case with  $\mathbf{R}_x = \mathbf{R}$ , the final terms in (14)  $\mathbf{F}_p \mathbf{R}^{-1} \mathbf{F}_p^{\text{H}}$  are

recognized from the maximal partial gains [47] or maximal extinction-cross section [43] in directions  $\hat{\mathbf{k}}_p$  and polarizations  $\hat{\mathbf{e}}_p$  corresponding to row  $p$  of  $\mathbf{F}$ .

The partial effective area  $A_{\text{eff}} = \lambda^2 G / (4\pi)$ , with the partial gain  $G$  in a direction  $\hat{\mathbf{k}}$  and polarization  $\hat{\mathbf{e}}$  is given by the partial radiation intensity normalized by the dissipated power and  $4\pi$  [31], [39]. Expressing the gain and effective area in the current matrix  $\mathbf{I}$ , resistance matrix  $\mathbf{R}$ , and radiation matrix  $\mathbf{F}_p$  yields a framework useful for optimization over the currents. The maximal partial effective area is determined from the solution of the optimization problem [47]

$$\begin{aligned} &\text{maximize} && A_{\text{eff},p} = \lambda^2 \mathbf{I}^{\text{H}} \mathbf{F}_p^{\text{H}} \mathbf{F}_p \mathbf{I} \\ &\text{subject to} && \mathbf{I}^{\text{H}} \mathbf{R} \mathbf{I} = 1, \end{aligned} \quad (15)$$

where  $\mathbf{F}_p \mathbf{I}$  is proportional to the  $\hat{\mathbf{e}}$ -component of the far field in the direction  $\hat{\mathbf{k}}$ , and  $\mathbf{I}^{\text{H}} \mathbf{F}_p^{\text{H}} \mathbf{F}_p \mathbf{I}$  to the corresponding partial radiation intensity [47]. The solution of (15) is

$$\max A_{\text{eff},p} = \lambda^2 \mathbf{F}_p^{\text{H}} \mathbf{R}^{-1} \mathbf{F}_p, \quad (16)$$

where the final terms in (14) are recognized. Inserting (16) into (14) produces the estimate

$$\sum_{n=1}^N \nu_n = \frac{1}{\lambda^2} \sum_{p=1}^{N_p} \Lambda_p^2 \max A_{\text{eff}}(\hat{\mathbf{k}}_p, \hat{\mathbf{e}}_p), \quad (17)$$

where by refining the quadrature rule over spatial points the sum approaches an integral

$$\sum_{n=1}^N \nu_n = \frac{1}{\lambda^2} \sum_{\hat{\mathbf{e}}=\{\hat{\theta}, \hat{\phi}\}} \int_{\Omega_R} A_{\text{eff}}(\hat{\mathbf{k}}, \hat{\mathbf{e}}) d\Omega_{\hat{\mathbf{k}}}, \quad (18)$$

which can also be expressed in the maximum gain. This expression resembles the NDoF for a circumscribing sphere [18], i.e., setting  $\Omega_R = 4\pi$ .

The generalized radiation modes  $\nu_n$  are related to the geometrical structure by observing that the maximal effective area in a direction  $\hat{\mathbf{k}}$  approaches the geometrical cross section,  $A_s(\hat{\mathbf{k}})$ , in the electrically large limit [47]  $\max A_{\text{eff}}(\hat{\mathbf{k}}) \approx A_s(\hat{\mathbf{k}})$ . This connects the generalized radiation modes and geometrical properties of the region  $\Omega_T$  with the maximal effective area (16) expressed solely in geometrical parameters producing the asymptotic NDoF

$$\sum_{n=1}^N \nu_n \approx \frac{2}{\lambda^2} \int_{\Omega_R} A_s(\hat{\mathbf{k}}) d\Omega_{\hat{\mathbf{k}}} = \frac{2A_{\text{TR}}}{\lambda^2}, \quad (19)$$

where the factor of two stems from the two polarizations  $\{\hat{\theta}, \hat{\phi}\}$ . The identity (19) relates the efficiency of the generalized radiation modes with the shadow area  $A_{\text{TR}}$ .

To estimate the NDoF, we assume that the efficiency of the generalized radiation modes separates into efficient modes and inefficient modes. This is similar to the decomposition of the channel eigenvalues  $\zeta_n$  in Fig. 3 which has approximately  $N_A$  modes  $\zeta_n N_A \approx 1$  and thereafter rapidly decreasing eigenvalues. The normalized modes  $\zeta_n$  are independent of the material loss (or similarly sampling density) but the channel eigenvalues increase as the sampling increases. The efficiency  $\nu_n$  of the generalized radiation modes diminish rapidly, similar to ordinary radiation modes [43]. Assuming that the efficient

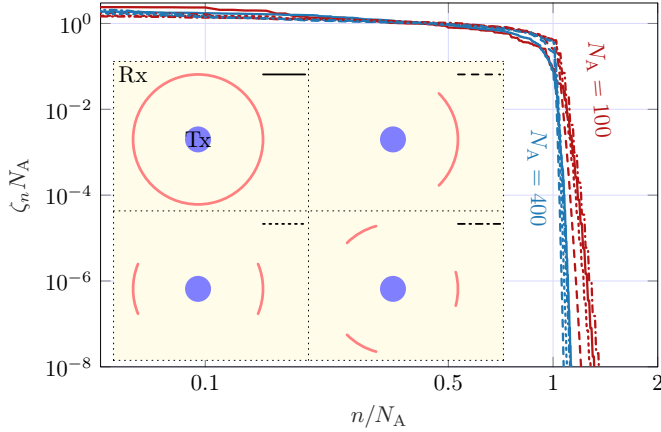


Figure 7. Normalized eigenvalues values  $\zeta_n$  for a cylindrical transmitter with radius  $a$  surrounded ( $2\pi$  coverage) by a cylindrical receiving region and a partly surrounding region ( $\pi/2$  coverage) as shown in the inset. The mode index is normalized with  $N_A$ .

generalized radiation modes have  $\nu_n \approx 1$  and inefficient modes have  $\nu_n \approx 0$  according to the ideal channel, see Fig. 3, resulting in efficiencies  $\nu_n$  according to

$$\nu_n \approx \begin{cases} 1 & n < N_A \\ 0 & n > N_A, \end{cases} \quad (20)$$

where  $N_A$  denotes the NDoF for the given shape and frequency. The transition from large to small modal efficiencies decreases with increasing electrical size, see Fig. 3. Assuming this ideal channel, inserted into (19) estimates the NDoF as

$$N_A = \frac{2A_{\text{TR}}}{\lambda^2} \quad \text{as } \lambda \rightarrow 0, \quad (21)$$

where the factor of two stems from the two polarizations of the EM field. The corresponding NDoF for 2D cases is

$$N_A = \frac{L_{\text{TR}}}{\lambda} \quad \text{as } \lambda \rightarrow 0, \quad (22)$$

where one polarization degree-of-freedom is assumed, *cf.*, (6).

These generalized radiation modes are slightly different from the modes induced by the decomposition of the channel matrix  $\mathbf{H}$  in (2) but is assumed to have similar NDoF. The mutual shadow length  $L_{\text{TR}}$  estimates the NDoF (22) as the shadow length measured in wavelength. This estimate is compared with numerical evaluation of the channel between  $\Omega_T$  and  $\Omega_R$ . This channel can be modelled in many ways, *e.g.*, point sources or expansion of a current density in basis functions. There is also a choice of using electric and/or magnetic current densities (single or double potentials). The presented results are for simplicity compared with the common model based on uniformly sampled ( $\Delta = \lambda/5$ ) point sources [19].

The mutual shadow length  $L_{\text{TR}}$  estimates the NDoF (22) as the shadow length measured in wavelength. This estimate is compared with numerical evaluation of the channel between  $\Omega_T$  and  $\Omega_R$ . To compare different configurations of transmitting and receiving regions, the singular values are evaluated for a fixed  $N_A$  by using (22) to set the wavelengths to

$$\lambda = L_{\text{TR}}/N_A. \quad (23)$$

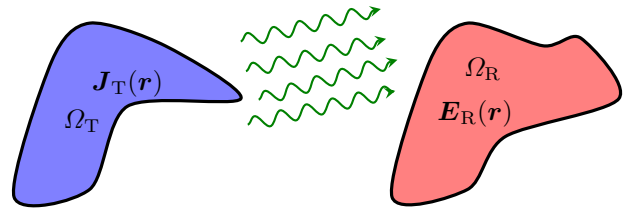


Figure 8. Communication channel represented by waves propagating in a direction  $\hat{\mathbf{k}}$  between transmitting and receiving regions.

The shadow length for cylindrical structures (circle) with radius  $a$  is  $L_{\text{TR}} = 2a \cdot 2\pi = 4\pi a$  which estimates the NDoF (22) to  $4\pi a/\lambda = 2ka$  which is consistent with the number of cylindrical waves using a cutoff  $ka$ . For a partly surrounding receiver, the shadow length is proportional to the angular coverage, *e.g.*, the  $\pi/2$  coverage depicted in Fig. 7 has shadow length  $\pi a$ . Normalized singular values  $\zeta_n$  for  $2\pi$  coverage and three cases of  $\pi/2$  coverage are shown in Fig. 7 using wavelengths (23) corresponding to NDoF  $N_A \in \{100, 400\}$ .

The transmitter is modelled as a solid circle (or cylinder) with radius  $a$ . Using (22) the NDoF  $N_A \in \{100, 400\}$  corresponds to  $a/\lambda = N_A a/L_{\text{TR}} \in \{8, 32\}$  for the circumscribed case and  $a/\lambda \in \{32, 127\}$  for the case with  $\pi/2$  coverage. Here, we note that all cases show a rapid transition from nearly constant eigenvalues  $\zeta_n N_A \approx 1$  for  $n < N_A$  to rapidly decaying eigenvalues for  $n > N_A$ . Moreover, the two  $N_A = 100$  and  $N_A = 400$  cases appear to separate, particularly the  $N_A = 400$  traces almost overlap for  $n > N_A$ .

The presented results are evaluated for receivers in the far field. The same setup is evaluated for a receiver region at a finite distance, *e.g.*, a receiver at radius  $5a$ , but the results are indistinguishable. This suggests that the same approach using rays (plane wave) can be used for object at finite distances.

## V. COMMUNICATION BETWEEN VOLUMES AND MUTUAL SHADOW AREA

To determine the asymptotic NDoF for communication between two arbitrary shaped regions, we take a similar approach and focus on the propagation of plane waves between the regions. This effectively reduce the question of NDoF to the question about the number of waves that can be supported between the objects. These waves are constructed by a plane-wave expansion of the current density over all directions. This procedure is depicted in Fig. 8, where plane waves (rays) in a direction  $\hat{\mathbf{k}}$  are illustrated. To communicate from  $\Omega_T$  to  $\Omega_R$  with a ray in the direction  $\hat{\mathbf{k}}$ , the ray needs to intersect both regions. The amount of interaction is proportional to the mutual area of this interaction. This is analogous to the shadow area for the far-field or circumscribing case in (6) and (21) which can be interpreted as a total interception of plane waves (rays) from directions described by  $\Omega_R$ .

A simple interpretation of this area comes from the mutual shadow area of the two objects, see Fig. 9. In this picture, the transmitting region  $\Omega_T$  illuminated by a plane wave in the direction  $\hat{\mathbf{k}}$  cast a shadow on the receiving region  $\Omega_R$ . This area can also be seen as the mutual shadow area of the two

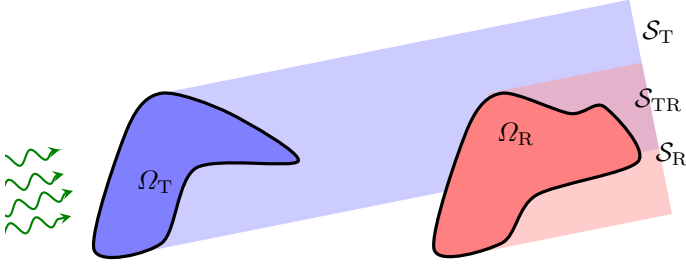


Figure 9. NDoF of the communication channel, represented by the mutual (intersection) shadow region from transmitting and receiving regions and a plane wave in the direction  $\hat{\mathbf{k}}$ .

shadows. This intersection area integrated for all directions is here shown to be proportional to the NDoF between the two regions in the asymptotic limit  $\lambda \rightarrow 0$ .

The total mutual shadow area is determined by integrating the mutual shadow area for all directions  $\hat{\mathbf{k}}$

$$L_{\text{TR}} = \int_0^{2\pi} |\mathcal{S}_{\text{TR}}(\phi)| d\phi \quad (24)$$

in  $\mathbb{R}^2$  and

$$A_{\text{TR}} = \int_{4\pi} |\mathcal{S}_{\text{TR}}(\hat{\mathbf{k}})| d\Omega_{\hat{\mathbf{k}}} \quad (25)$$

in  $\mathbb{R}^3$ , where the shadow region is determined from  $\Omega_T$  to  $\Omega_R$ , *i.e.*, the shadow from  $\Omega_R$  onto  $\Omega_T$  is not included. In (24) and (25)  $|\mathcal{S}_{\text{TR}}|$  denotes the mutual shadow area (length) for a given direction of illumination. Here, we also note that the mutual shadow area can alternatively be determined from the difference between the sum of the shadow areas of  $\Omega_T$  and  $\Omega_R$  minus the shadow area of the composed object  $\Omega_{\text{TR}}$ . The NDoF for communication between systems confined to those regions are approximately

$$N_A = \begin{cases} L_{\text{TR}}/\lambda & \text{in } \mathbb{R}^2 \\ A_{\text{TR}}/\lambda^2 & \text{in } \mathbb{R}^3 \end{cases} \quad (26)$$

in agreement with (22) and (21). These estimates (26) of the asymptotic number of propagating modes for (scalar) Helmholtz equation are doubled for Maxwell's equations when two orthogonal polarizations contribute. These NDoF reduces to many previously known cases for those specific geometries, *e.g.*, the case with a receiving spherical region circumscribing the transmitter (6) and paraxial approximation (7).

Evaluation of shadows is well-developed in computer graphics [48]. Shadows for canonical shapes can be evaluated semi-analytically, while shadows for objects described by a mesh can be determined numerically by combining the shadows of each mesh element.

To illustrate shadow and mutual shadow areas, two spherical regions with radii  $a_T \geq a_R$  separated by a distance  $h$  as depicted in Fig. 10 are considered. The spheres are, without loss of generality, placed on the  $z$ -axis, producing a body of revolution (BoR) object with the incident illumination parametrized by the polar angle  $\theta$ . The shadow areas are

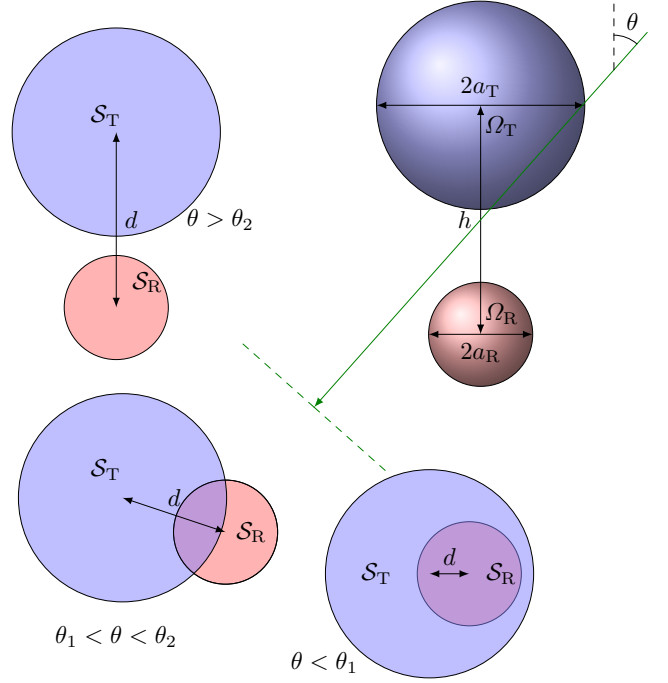


Figure 10. Illustration of the shadow and mutual shadow from two spheres with radii  $a_T$  and  $a_R \leq a_T$  separated a distance  $d$ . The spheres are placed on the  $\hat{z}$ -axis and illuminated from a direction  $\hat{\mathbf{k}}$  described by the polar angle  $\theta$ . The shadow of  $\Omega_R$  is contained within the shadow of  $\Omega_T$  for small  $\theta < \theta_1$ , intersects the shadow for  $\theta_1 \leq \theta \leq \theta_2$ , and are disjoint for  $\theta > \theta_2$ .

determined on a plane perpendicular to the direction of illumination.

The shadow of each sphere is a circular disc with the same radius as the sphere. The two shadows can overlap, partly overlap, or being separated depending on the illumination angle  $\theta$  related to the distance  $d = h \sin \theta$  between the disc centers. The shadow  $\mathcal{S}_R$  is inside the shadow of  $\mathcal{S}_T$  for sufficiently small polar angles  $\theta < \theta_1$ , see App. C for details. This gives a mutual shadow area  $\pi a_R^2$ . For larger polar angles  $\theta_1 < \theta < \theta_2$ , the two shadows partly overlap, with a mutual shadow area given in App. C. As the polar angle increases  $\theta > \theta_2$ , the two shadows separate, and the mutual shadow area vanish. For non-intersecting shadows, it is not possible to communicate between the regions using rays with this propagation direction.

As the polar angle  $\theta$  approaches  $\pi$ , there is a corresponding mutual shadow area from the receiving region  $\Omega_R$  onto the transmitting region  $\Omega_T$ . This mutual shadow area has the same size but is not accounted for in the shadow area from  $\Omega_T$  to  $\Omega_R$  in (25).

The mutual shadow areas  $|\mathcal{S}_{\text{TR}}(\theta)|$  have simple analytical expressions and the total mutual shadow area  $A_{\text{TR}}$  is determined by integration of  $|\mathcal{S}_{\text{TR}}(\theta)|$  over  $[0, \theta_2]$  weighted by  $2\pi \sin \theta$  from integration over the azimuthal angle  $\phi$  of the spherical coordinate system.

Shadow lengths are also straight forward to evaluate in 2D. Starting with two line objects as depicted in Fig. 11 and detailed in App. B. The shadow from a line object is an interval with endpoints determined from the projection of the endpoints on a line  $\hat{\mathbf{p}}$  perpendicular to the direction of the illumination,

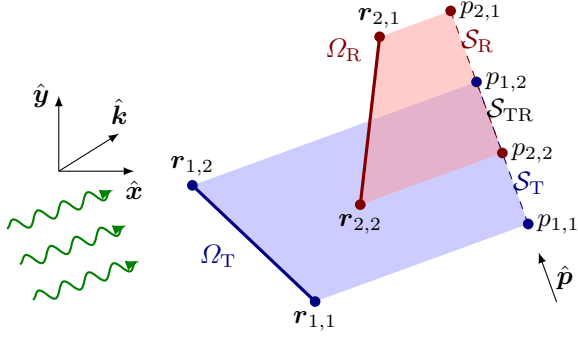


Figure 11. Mutual shadow length between two line objects in  $\mathbb{R}^2$  illuminated from direction  $\hat{\mathbf{k}}$  described by an angle  $\phi$ . The shadow is projected on a line perpendicular to  $\hat{\mathbf{k}}$ .

*i.e.*,  $\hat{\mathbf{p}} \cdot \hat{\mathbf{k}} = 0$ . The intersection length is finally determined from the intersection of the shadow intervals, see App. B for details.

## VI. NDOF AND SHADOW LENGTH IN 2D

To illustrate NDoF and shadow length, consider first two parallel lines with lengths  $\ell_1$  and  $\ell_2$  separated by a distance  $d$  as shown in the inset of Fig. 12. The mutual shadow length is determined by integrating  $|\mathcal{S}_{\text{TR}}(\phi)|$  over all illumination directions  $\phi$ , with the transmitter casting a shadow on the receiver

$$2 \int_0^{\phi_1} \ell_2 \cos \phi \, d\phi + 2 \int_{\phi_1}^{\phi_2} \frac{\ell_1 + \ell_2}{2} \cos \phi - d \sin \phi \, d\phi \quad (27)$$

with  $\tan \phi_1 = \delta$  and  $\tan \phi_2 = \beta$ , where  $\delta = |\ell_1 - \ell_2|/(2d)$  and  $\beta = (\ell_1 + \ell_2)/(2d)$ . Integration over  $\phi$  leads to the total shadow length

$$L_{\text{TR}} = 2d(\sqrt{1 + \beta^2} - \sqrt{1 + \delta^2}) \approx \begin{cases} 2 \min\{\ell_1, \ell_2\}, & d \rightarrow 0 \\ \ell_1 \ell_2 / d, & d \rightarrow \infty, \end{cases} \quad (28)$$

where the paraxial result (7) is recovered as  $d \rightarrow \infty$  and Weyl's law for  $d \ll \ell$ , with a factor 1/2 due to radiation in one direction.

Different configurations of transmitting and receiving regions are compared by evaluating the eigenvalues of the channel correlation matrix for a fixed  $N_A$  by setting the wavelength to  $\lambda = L_{\text{TR}}/N_A$  and using uniformly sampled point sources with  $\Delta = \lambda/5$  [19].

The results in Fig. 12 show the normalized eigenvalues  $\zeta_n$  in (3) of the resulting channel matrix for  $N_A \in \{5, 10, 50, 100\}$  and distances  $d/\ell \in \{0.1, 0.5, 1, 5\}$ . The NDoF  $N_A$  is evaluated using (28) as depicted in the inset of Fig. 12. The considered cases  $d/\ell \in \{0.1, 0.5, 1, 5\}$  are indicated by markers. Small distances have mutual shadow lengths  $L_{\text{TR}} \approx \ell$  corresponding to twice the shorter strip length (28). The shadow length decreases with the distances and approximates the paraxial approximation as  $d/\ell \rightarrow \infty$ . For  $d/\ell = 5$ , the shadow length  $L_{\text{TR}} \approx \ell/10$  implies a tenfold decrease in the NDoF for a fixed wavelength compared to the  $d \ll \ell$  case. The electrical size varies between  $\ell/\lambda \approx 5$  for  $N_A = 5$  and  $d/\ell = 0.1$  to  $\ell/\lambda \approx 1000$  for  $N_A = 100$  and

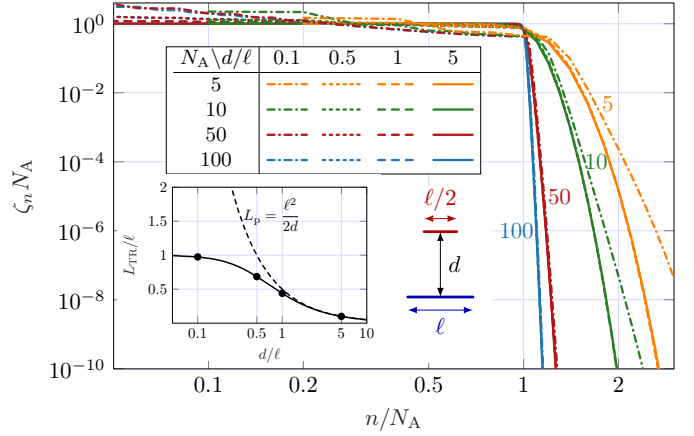


Figure 12. Normalized singular values  $\zeta_n$  for two lines with length  $\ell$  and  $\ell/2$  separated a distance  $d$ . The mode index is normalized with  $N_A$  determined from the mutual shadow length (28).

$d/\ell = 5$ . The singular value index  $n$  on the horizontal axis is scaled with the NDoF  $N_A$ .

The normalized eigenvalues  $\zeta_n$  are approximately equal to  $1/N_A$  for  $n < N_A$ . A 'corner' in the singular values is observed around  $n \approx N_A$ . For indices  $n > N_A$ , the singular values  $\zeta_n$  decay rapidly, particularly for large  $N_A$ . This sharp transition from an almost constant  $\zeta_n N_A \approx 1$  to a rapidly decaying  $\zeta_n$  is used to define a NDoF, here denoted  $N_c$ . This implies that there are  $N_c$  modes with approximately the same performance, and the performance decreases rapidly if additional modes are used, indicating a very high cost to use more than  $N_c$  modes. The results show that this 'corner' becomes more pronounced as the electrical size increases, or more precisely, as the NDoF increases.

The results in Fig. 12 indicate a strong correlation between the NDoF estimates from the shadow area  $N_A$  and from the corner of the eigenvalue distribution  $N_c$ . They also show that the distribution of the eigenvalues  $\zeta_n$  primarily depends on  $N_A$ . The curves for the same  $N_A$  but different distances  $d/\ell$  overlap, except for the short distance  $d = 0.1\ell$  and low  $N_A \in \{5, 10\}$ . These cases correspond to a separation between the transmitting and receiving regions  $d/\lambda = N_A d/\ell \in \{0.5, 1\}$ , which is on the order of a wavelength. The results coincide for larger  $N_A$  corresponding to shorter wavelengths, supporting  $N_A$  as the NDoF as  $\lambda \rightarrow 0$ . For sub-wavelength distances, the NDoF can be higher due to strong reactive coupling [23].

The broadside configuration maximizes the mutual shadow length. Rotating one of the lines reduces this length. Consider a setup with two lines, one of length  $\ell$  and the other  $\ell/2$ , separated by a distance  $\ell/2$  and rotated by an angle  $\phi$ , as shown in the inset of Fig. 13. The mutual shadow length is evaluated as described in App. B. The mutual shadow length vanishes for the endfire configuration ( $\phi = \pi/2$ ), at which the estimate (26) becomes invalid. The mutual shadow lengths  $L_{\text{TR}}$  are plotted in Fig. 13 for  $\phi \in \{0, \pi/9, 2\pi/9\}$ . Additionally, a setup with rectangular regions is included in Fig. 13.

Normalized singular values  $\zeta_n$  are depicted in Fig. 14 for  $N_A \in \{5, 10, 50, 100\}$  and the nine configurations shown

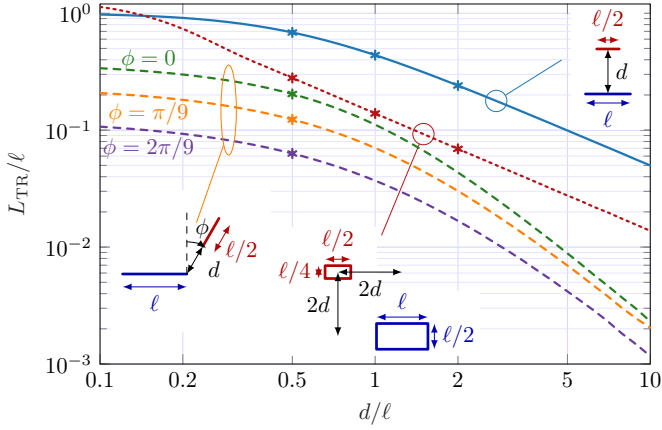


Figure 13. Normalized shadow lengths for parallel lines (solid), rotated lines (dashed), and separated rectangles (dotted).

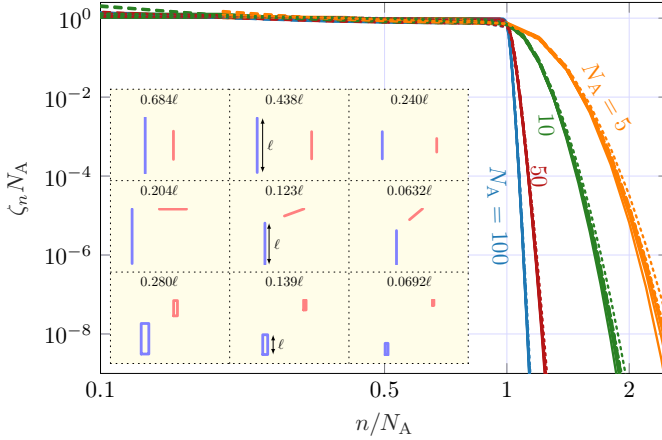


Figure 14. Normalized eigenvalues values  $\zeta_n$  for the nine different configurations shown in the inset using wavelengths  $\lambda = L_{\text{TR}}/N_A$ . The mode index is normalized with  $N_A$ . Parallel lines as in Fig. 12 (solid curves), rotated lines (dashed lines), and rectangles (dotted lines) with separation distances indicated by the line thickness, see markers in Fig. 13.

in the inset and in Fig. 13. Normalizing by  $N_A$  groups the curves for the different configurations, indicating that the mutual shadow length is a fundamental parameter for the NDoF and the distribution of the eigenvalues. The spread within each group decreases as  $N_A$  increases, and the different configurations for the  $N_A = 100$  case overlap for  $n > N_A$ .

The results in Fig. 14 depend slightly on the specific configuration and the point source model used for the channel matrix. This dependence can be attributed to the symmetry of the point source model, where the radiated field from a point source is isotropic. Consequently, the radiated field from a line region is symmetric in directions away from the line, reducing the NDoF. However, this symmetry is broken for regions with an inner region, such as an area in 2D or a volume in 3D. The symmetry is also broken by using both electric and magnetic current sources for electromagnetic fields [18], similar to single and double layer potentials for scalar fields.

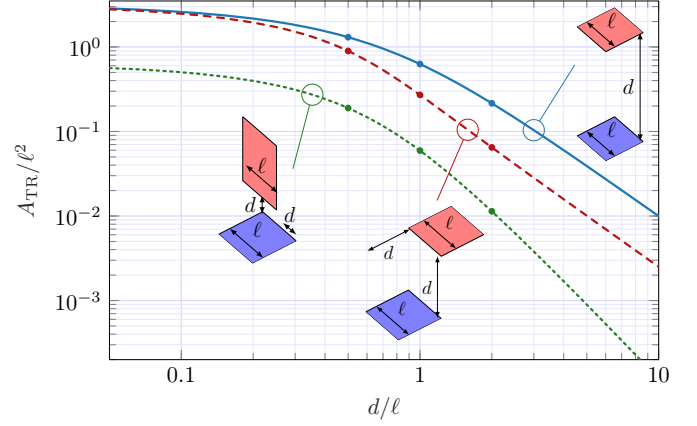


Figure 15. Mutual shadow area in units of  $\ell^2$  for communication between two square regions with side length  $\ell$  using setups as depicted in the insets.

## VII. NDOF AND SHADOW AREA IN 3D

Shadow areas in 3D are also easily evaluated for arbitrary shaped regions using numerical techniques. Consider for simplicity a geometry composed by  $N$  convex shapes,  $n = 1, \dots, N$ , each described by a set of points  $\mathbf{r}_{np}$ ,  $p = 1, \dots, N_p$ . This can *e.g.*, be a surface mesh with node points. Using spherical coordinates with the illuminating direction defined by the radial direction,  $\hat{\mathbf{r}}$ , we project the shadow on the orthogonal plane spanned by the unit vectors  $\hat{\boldsymbol{\theta}}$  and  $\hat{\boldsymbol{\phi}}$ , see Fig. 10. Using standard algorithms to find the convex hull of this set of points, *e.g.*, `convhull` in `matlab`. This produces polygon-like shapes in 2D, for which it is easy to construct unions and intersections. Note that shadow areas can be determined in many ways, and that determining shadows is a standard procedure in computer vision [48].

Mutual shadow area for three configurations using square plates with side lengths  $\ell$  are depicted in Fig. 15. Parallel plates separated a distance  $d$ , similar to the setup in Fig. 3, are shown with a solid line. The mutual shadow area approaches  $A_{\text{TR}} \approx \pi \ell^2$  for  $d \ll \ell$  according to a half of Weyl's law (5). For larger distances, it approaches the paraxial approximation  $A_{\text{TR}} \approx \ell^4/d^2$ .

Combining the vertical separation with a transverse shift is illustrated by the dashed curve. The effect of the transverse shift is negligible compared with the vertical shift for  $d \ll \ell$ , but its impact increases for  $d > \ell$ . This is partly explained by the reduced shadow due to the projection of the planar regions along a  $45^\circ$  angle and the increased distance which together reduces the mutual shadow area approximately a factor of 4 for  $d \gg \ell$ . The dotted line illustrates the case with one rectangle rotated  $90^\circ$ , demonstrating an end-fire configuration. This reduces the mutual shadow area, both for small and large distances. Note that the mutual shadow area vanishes for an end-fire setup of two plates in the same plane, producing a different scaling.

Normalized eigenvalues  $\zeta_n$  for the setups in Fig. 15 using  $d/\ell \in \{0.5, 1, 2\}$  and  $N_A \in \{50, 100, 200\}$  are shown in Fig. 16. The different setups are separated by solid, dashed, and dotted line styles as in Fig. 15 and line widths for distances. The results show that  $\zeta_n N_A \approx 1$  for  $n < N_A$  and

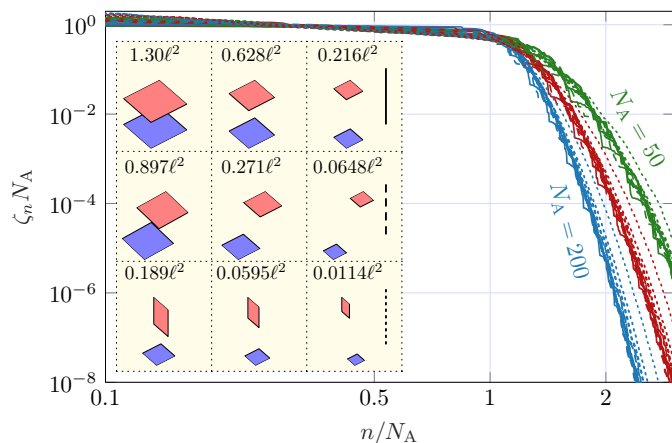


Figure 16. Normalized eigenvalue values  $\zeta_n$  of the channel matrix for communication between nine configurations for two square regions with side length  $\ell$  evaluated for  $N_A \in \{50, 100, 200\}$ . The setups are depicted in the inset together with its mutual shadow area in units of  $\ell^2$  for the distances  $d/\ell \in \{0.5, 1, 2\}$  in Fig. 15.

that the curves cluster for different  $N_A$  for  $n > N_A$ . The slopes of the eigenvalues are less steep than for the corresponding 2D cases in Fig. 14. This is partly explained by the distribution of the DoF over two orthogonal directions.

Evaluation of the channel for fixed NDoF  $N_A$  case corresponds to evaluation of the channel for different wavelengths. The top left case in Fig. 16 has a mutual shadow area of  $A_{TR} \approx 1.3\ell^2$  which for the  $N_A = 200$  case imply  $\ell^2/\lambda^2 = N_A \ell/A_{TR} \approx 154$ . Using 5 sample points per wavelength produces a channel matrix with dimension  $N_T = N_R \approx 4 \cdot 10^3$ . This is easily handled on a standard PC. The corresponding bottom right case has a much smaller mutual shadow area  $A_{TR} \approx 0.0114\ell^2$  which produces a channel matrix of dimension  $N_T = N_R \approx 4 \cdot 10^5$ .

For these large dimensions, storage of  $\mathbf{H}$  and evaluation of singular values or eigenvalues are challenging. However, using the low-rank property of the channel matrix  $\mathbf{H}$ , *i.e.*,  $\text{rank}(\mathbf{H}) \approx N_A \ll \min\{N_T, N_R\}$  is much smaller than the dimension of  $\mathbf{H}$  opens for *e.g.*, evaluations based on randomized SVD [28].

Randomized SVD is an effective approach to evaluate the dominant singular values of low-rank matrices [28] and can be applied to evaluate  $\text{svd}(\mathbf{H})$ , and hence  $\zeta_n$ . Moreover, the randomized SVD is matrix-free, meaning that the full channel matrix is not needed for the evaluation of the singular values. This makes it suitable for cases with very large dimensions of  $\mathbf{H}$ , when  $\lambda \rightarrow 0$ . The matrix-free randomized SVD can be interpreted as evaluating the received signals for a set of random excitations.

The rank of the channel matrix can be approximated by  $N_A$ . By constructing a  $N_T \times P$  random matrix  $\mathbf{A}$  with, for example,  $P = 3N_A$ , the received signals  $\mathbf{Y} = \mathbf{H}\mathbf{A}$  can be evaluated, where  $\mathbf{Y}$  has dimensions  $N_T \times P$ , without evaluation of  $\mathbf{H}$ . An orthonormal basis  $\mathbf{W}$  of  $\mathbf{Y}$  is then retransmitted through the adjoint channel, which is evaluated by exciting the channel from the receiver side using  $\mathbf{W}^*$ , *i.e.*,  $\mathbf{B} = \mathbf{W}^H \mathbf{H} = (\mathbf{H}^T \mathbf{W}^*)^T$ . This final matrix  $\mathbf{B}$  is of size  $P \times P$

and is therefore easy to evaluate using an ordinary SVD, *i.e.*,  $\text{svd}(\mathbf{B})$ . Its singular values approximate the dominant singular values of  $\text{svd}(\mathbf{H})$  [28] and hence square roots the eigenvalues  $\sigma_n$  in (3).

## VIII. CONCLUSIONS

This study demonstrates that the asymptotic NDoF for communication between regions is approximated by the mutual shadow area of the regions when measured in wavelengths. This analytical estimate provides valuable physical insights and complements numerical evaluations. The numerical results reveal that the eigenvalues of the channel are approximately constant up to the NDoF, after which they decay rapidly. Additionally, it is observed that the normalized eigenvalues of the channel correlation matrix tend to cluster for different setups with the same NDoF. The use of randomized singular value decomposition enables the evaluation of eigenvalues for the correlation matrix, facilitating simulations for setups with small wavelengths. The presented theory and results enhance the understanding of communication system performance in various setup of transmitter and receiver geometries in a free-space propagation environment.

The results presented here primarily focus on simple setups involving lines and plates. However, the approach is versatile and can be applied to arbitrarily shaped regions, including non-convex and non-connected geometries. In setups with symmetries, it may be necessary to consider both electric and magnetic current densities. The generalized radiation modes, derived from the radiated field over a finite far-field region, are also directly applicable to the study of characteristic modes. This framework facilitates the examination of the NDoF for fixed structures, offering valuable insights into their performance and behavior.

## APPENDIX A CURRENT DENSITY

The current density  $\mathbf{J}(\mathbf{r})$  in  $\Omega_T$  is expanded in a set of basis functions  $\psi_n(\mathbf{r})$  [31]

$$\mathbf{J}(\mathbf{r}) = \sum_{n=1}^{N_T} I_n \psi_n(\mathbf{r}). \quad (29)$$

These basis functions can be local, such as divergence conforming or point sources, or global such as spherical waves. The least-squares,  $L^2$ , norm of the current density is

$$\int |\mathbf{J}|^2 dV = \sum_{mn} I_m^* I_n \int \psi_m(\mathbf{r}) \cdot \psi_n(\mathbf{r}) dV = \mathbf{I}^H \mathbf{\Psi} \mathbf{I}, \quad (30)$$

where  $\mathbf{\Psi}$  denotes the Gram matrix [33]. The  $L^2$  norm is not defined for point sources, but for sub-wavelength sampling, it is possible to consider the point sources as an approximation of pulse basis functions, *i.e.*, constant basis functions with unit volume (area). For the case with uniform sampling using point sources, the Gram matrix is proportional to the identity matrix. Homogeneous material losses modeled with a resistivity  $\rho_r$  are described by a material loss matrix  $\mathbf{R}_\rho = \rho_r \mathbf{\Psi}$  meaning that current norm (30) and material losses are related.

The radiated field from the current density is determined by a convolution with a Green's function. The used scalar Green's function in  $\mathbb{R}^2$  and  $\mathbb{R}^3$  are

$$G_2(\mathbf{r} - \mathbf{r}') = \frac{j}{4} H_0(k|\mathbf{r} - \mathbf{r}'|) \quad \text{and} \quad G_3 = \frac{e^{-jk|\mathbf{r} - \mathbf{r}'|}}{4\pi|\mathbf{r} - \mathbf{r}'|}, \quad (31)$$

respectively, and the Green's dyadic  $\mathbf{G} = (\mathbf{1} + k^{-2}\nabla\nabla)G_3$ .

## APPENDIX B MUTUAL SHADOW LENGTH

The mutual shadow length from a set of lines described by their end points  $\mathbf{r}_{mn}$ , with  $m \in \{T, R\}$  is determined for an illumination in the  $\hat{\mathbf{k}}$ -direction, using a plane wave  $E_z(\mathbf{r}) = e^{-jk\hat{\mathbf{k}}\cdot\mathbf{r}}$  polarized in the  $\hat{\mathbf{z}}$ -direction, see Fig. 11. The shadow is projected on a line perpendicular to  $\hat{\mathbf{k}} = \hat{\mathbf{x}} \cos(\phi) + \hat{\mathbf{y}} \sin(\phi)$ , which using polar coordinates with azimuth angle  $\phi$  results in

$$\hat{\mathbf{p}} = -\hat{\mathbf{x}} \sin(\phi) + \hat{\mathbf{y}} \cos(\phi). \quad (32)$$

Projecting the node points on the  $\hat{\mathbf{p}}$ -line produces a set of numbers  $p_{mn} = \hat{\mathbf{p}} \cdot \mathbf{r}_{mn}$  and the lines a set of intervals  $I_m = [\min_n p_{mn}, \max_n p_{mn}]$ . The mutual shadow is formed by  $I_1 \cap I_2$ . The intersection is empty if  $\max_n p_{mn} \leq \min_n p_{qn}$  for some  $m \neq q$ , i.e.,

$$\max_n \{p_{1n}\} \leq \min_n \{p_{2n}\} \quad \text{or} \quad \max_n \{p_{2n}\} \leq \min_n \{p_{1n}\}. \quad (33)$$

The length of the interval is finally

$$|\mathcal{S}_{\text{TR}}| = \max_n \{p_{1n}\} - \min_n \{p_{2n}\} \quad (34)$$

or

$$|\mathcal{S}_{\text{TR}}| = \max_n \{p_{2n}\} - \min_n \{p_{1n}\}. \quad (35)$$

The total mutual shadow length is determined by integration (24).

## APPENDIX C NDOF AND SHADOW AREA FOR TWO SPHERES

Shadow area and mutual shadow area are illustrated for two spheres having radii  $a_n$ ,  $n = 1, 2$  and separated a distance  $h$ , see Fig. 10. The spheres are without loss of generality placed on the  $z$ -axis producing a BoR object with an incident illumination parametrized by the polar angle  $\theta$ .

The shadow of each sphere is a circular disc with the same radius as the sphere. The two shadows can overlap, partly overlap, or being separated depending on the illumination angle  $\theta$  through the distance  $d = h \sin \theta$ . For  $0 \leq \theta \leq \theta_1$  with

$$\sin \theta_1 = |a_1 - a_2|/h \quad (36)$$

the two shadows overlap, as illustrated in the bottom part of Fig. 10. For  $\theta_1 < \theta < \theta_2$  with

$$\sin \theta_2 = (a_1 + a_2)/h \quad (37)$$

the two shadows partly overlap. And for  $\theta_2 \leq \theta \leq \pi/2$  the two shadows are separated. This behavior is repeated symmetrically for  $\pi/2 \leq \theta \leq \pi$ .

The total shadow area is determined by integrating over all incident angles, which reduces to a line integral over

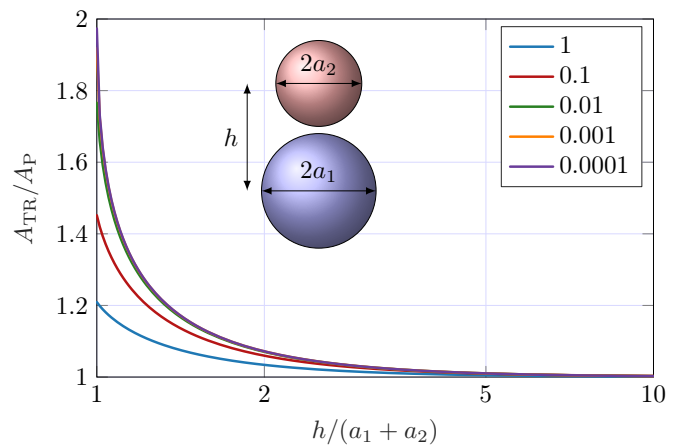


Figure 17. Mutual shadow area for two spheres with radii  $a_1$  and  $a_2$  normalized by the paraxial approximation (41).

$[0, \pi/2]$  for this specific case. For the mutual shadow area, it is sufficient to integrate over  $[0, \theta_2]$ . The mutual area for  $\theta < \theta_1$  is  $\pi a_1^2$  giving

$$A = 2\pi^2 \min\{a_n^2\} (1 - \cos \theta_1) + 2\pi \int_{\theta_1}^{\theta_2} A(\theta) \sin \theta d\theta. \quad (38)$$

The partly overlapping shadow area is divided into two parts  $A = A_1 + A_2$  determined as

$$A_n = a_n^2 (\text{acos}(d_n) - d_n \sqrt{1 - d_n^2}) \quad (39)$$

with

$$d_n = (d^2 + 2a_n^2 - a_1^2 - a_2^2)/(2da_n) \quad (40)$$

The integral simplify for two equal spheres  $a_1 = a_2$  and can be expressed in elliptic integrals, however it is also trivially solved by numerical quadrature, see Fig. 17. The mutual shadow area is normalized by the paraxial approximation

$$A_P = \frac{A_1 A_2}{h^2} = \frac{\pi^2 a_1^2 a_2^2}{h^2}, \quad (41)$$

which approximated the mutual shadow area very well for distances  $h > 2(a_1 + a_2)$ , see Fig. 17.

## REFERENCES

- [1] A. Pizzo, A. de Jesus Torres, L. Sanguinetti, and T. L. Marzetta, "Nyquist sampling and degrees of freedom of electromagnetic fields," *IEEE Trans. Signal Process.*, vol. 70, pp. 3935–3947, 2022.
- [2] S. Hu, F. Rusek, and O. Edfors, "Beyond massive MIMO: The potential of data transmission with large intelligent surfaces," *IEEE Trans. Signal Process.*, vol. 66, no. 10, pp. 2746–2758, 2018.
- [3] M. D. Migliore, "On the role of the number of degrees of freedom of the field in MIMO channels," *IEEE Trans. Antennas Propag.*, vol. 54, no. 2, pp. 620–628, Feb 2006.
- [4] M. Migliore, "On electromagnetics and information theory," *IEEE Trans. Antennas Propag.*, vol. 56, no. 10, pp. 3188–3200, Oct. 2008.
- [5] M. Franceschetti, *Wave theory of information*. Cambridge University Press, 2017.
- [6] E. Björnson, C.-B. Chae, R. W. Heath Jr, T. L. Marzetta, A. Mezghani, L. Sanguinetti, F. Rusek, M. R. Castellanos, D. Jun, and Ö. T. Demir, "Towards 6G MIMO: Massive spatial multiplexing, dense arrays, and interplay between electromagnetics and processing," *arXiv preprint arXiv:2401.02844*, 2024.
- [7] A. S. Poon, R. W. Brodersen, and D. N. Tse, "Degrees of freedom in multiple-antenna channels: A signal space approach," *IEEE Trans. Information Theory*, vol. 51, no. 2, pp. 523–536, 2005.

- [8] M. Franceschetti, M. D. Migliore, and P. Minero, "The capacity of wireless networks: Information-theoretic and physical limits," vol. 55, no. 8, pp. 3413–3424, Aug. 2009.
- [9] G. T. Di Francia, "Resolving power and information," *JOSA*, vol. 45, no. 7, pp. 497–501, 1955.
- [10] —, "Directivity, super-gain and information," *IRE Trans. Antennas and Propag.*, vol. 4, no. 3, pp. 473–478, 1956.
- [11] O. M. Bucci and G. Franceschetti, "On the degrees of freedom of scattered fields," *IEEE Trans. Antennas Propag.*, vol. 37, no. 7, pp. 918–926, 1989.
- [12] O. Bucci and T. Isernia, "Electromagnetic inverse scattering: Retrievable information and measurement strategies," *Radio science*, vol. 32, no. 6, pp. 2123–2137, 1997.
- [13] P.-S. Kildal, E. Martini, and S. Maci, "Degrees of freedom and maximum directivity of antennas: A bound on maximum directivity of nonsuper-reactive antennas," *IEEE Antennas Propag. Mag.*, vol. 59, no. 4, pp. 16–25, 2017.
- [14] D. A. Hill, "Electronic mode stirring for reverberation chambers," *IEEE Trans. Electromagn. Compat.*, vol. 36, no. 4, pp. 294–299, 1994.
- [15] R. Janaswamy, "On the EM degrees of freedom in scattering environments," *IEEE Trans. Antennas Propag.*, vol. 59, no. 10, pp. 3872–3881, 2011.
- [16] H. Weyl, "Über die asymptotische verteilung der eigenwerte," *Nachrichten von der Gesellschaft der Wissenschaften zu Göttingen, Mathematisch-Physikalische Klasse*, vol. 1911, pp. 110–117, 1911.
- [17] W. Arendt, R. Nittka, W. Peter, and F. Steiner, "Weyl's law: Spectral properties of the Laplacian in mathematics and physics," *Mathematical analysis of evolution, information, and complexity*, pp. 1–71, 2009.
- [18] M. Gustafsson, "Degrees of freedom for radiating systems," *arXiv preprint arXiv:2404.08976*, 2024.
- [19] R. Piestun and D. A. Miller, "Electromagnetic degrees of freedom of an optical system," *JOSA A*, vol. 17, no. 5, pp. 892–902, 2000.
- [20] D. A. Miller, "Waves, modes, communications, and optics: a tutorial," *Advances in Optics and Photonics*, vol. 11, no. 3, pp. 679–825, 2019.
- [21] M. A. Jensen and J. W. Wallace, "Capacity of the continuous-space electromagnetic channel," *IEEE Trans. Antennas Propag.*, vol. 56, no. 2, pp. 524–531, 2008.
- [22] S. Nordebo, M. Gustafsson, and G. Kristensson, "On the capacity of the free space antenna channel," in *IEEE Antennas and Propagation Society International Symposium 2006*, IEEE Press, 2006, pp. 3105–3108.
- [23] R. Ji, S. Chen, C. Huang, J. Yang, E. Wei, Z. Zhang, C. Yuen, and M. Debbah, "Extra DoF of near-field holographic MIMO communications leveraging evanescent waves," *IEEE Wirel. Commun. Lett.*, vol. 12, no. 4, pp. 580–584, 2023.
- [24] S. S. Yuan, J. Wu, H. Xu, T. Wang, D. Li, X. Chen, C. Huang, S. Sun, S. Zheng, X. Zhang *et al.*, "Breaking the degrees-of-freedom limit of holographic MIMO communications: A 3-D antenna array topology," *IEEE Trans. Veh. Technol.*, 2024.
- [25] S. S. Yuan, Z. He, X. Chen, C. Huang, and E. Wei, "Electromagnetic effective degree of freedom of an MIMO system in free space," *IEEE Antennas Wirel. Propag. Lett.*, vol. 21, no. 3, pp. 446–450, 2022.
- [26] M. D. Migliore, "Horse (electromagnetics) is more important than horse-man (information) for wireless transmission," *IEEE Trans. Antennas Propag.*, vol. 67, no. 4, pp. 2046–2055, 2019.
- [27] J. C. Ruiz-Sicilia, M. Di Renzo, M. D. Migliore, M. Debbah, and H. V. Poor, "On the degrees of freedom and eigenfunctions of line-of-sight holographic MIMO communications," *arXiv preprint arXiv:2308.08009*, 2023.
- [28] N. Halko, P.-G. Martinsson, and J. A. Tropp, "Finding structure with randomness: Probabilistic algorithms for constructing approximate matrix decompositions," *SIAM review*, vol. 53, no. 2, pp. 217–288, 2011.
- [29] A. Paulraj, R. Nabar, and D. Gore, *Introduction to Space-Time Wireless Communications*. Cambridge: Cambridge University Press, 2003.
- [30] A. F. Molisch, *Wireless Communications*, 2nd ed. New York, NY: John Wiley & Sons, 2011.
- [31] R. F. Harrington, *Field Computation by Moment Methods*. New York, NY: Macmillan, 1968.
- [32] D.-S. Shiu, G. J. Foschini, M. J. Gans, and J. M. Kahn, "Fading correlation and its effect on the capacity of multielement antenna systems," *IEEE Trans. on Communication*, vol. 48, no. 3, pp. 502–513, Mar. 2000.
- [33] R. A. Horn and C. R. Johnson, *Topics in Matrix Analysis*. Cambridge University Press, 1991.
- [34] J. A. Stratton, *Electromagnetic Theory*. New York, NY: McGraw-Hill, 1941.
- [35] G. Kristensson, *Scattering of Electromagnetic Waves by Obstacles*. Edison, NJ: SciTech Publishing, an imprint of the IET, 2016.
- [36] M. Gustafsson and S. Nordebo, "On the spectral efficiency of a sphere," *Prog. Electromagn. Res.*, vol. 67, pp. 275–296, 2007.
- [37] M. Gustafsson and J. Lundgren, "Degrees of freedom and characteristic modes," *IEEE Antennas Propag. Mag.*, pp. 2–12, 2024, (in press).
- [38] R. Harrington, "On the gain and beamwidth of directional antennas," *IEEE Trans. Antennas Propag.*, vol. 6, no. 3, pp. 219–225, 1958.
- [39] W. L. Stutzman and G. A. Thiele, *Antenna Theory and Design*, 2nd ed. New York, NY: John Wiley & Sons, 1998.
- [40] V. Vouk, "Projected area of convex bodies," *Nature*, vol. 162, no. 4113, pp. 330–331, 1948.
- [41] M. Capek, J. Lundgren, M. Gustafsson, K. Schab, and L. Jelinek, "Characteristic mode decomposition using the scattering dyadic in arbitrary full-wave solvers," *IEEE Trans. Antennas Propag.*, vol. 71, no. 1, pp. 830–839, 2023.
- [42] C. Ehrenborg and M. Gustafsson, "Physical bounds and radiation modes for MIMO antennas," *IEEE Trans. Antennas Propag.*, vol. 68, no. 6, pp. 4302–4311, 2020.
- [43] M. Gustafsson, K. Schab, L. Jelinek, and M. Capek, "Upper bounds on absorption and scattering," *New Journal of Physics*, vol. 22, no. 073013, 2020.
- [44] C. Ehrenborg and M. Gustafsson, "Fundamental bounds on MIMO antennas," *IEEE Antennas Wireless Propag. Lett.*, vol. 17, no. 1, pp. 21–24, January 2018.
- [45] C. Ehrenborg, M. Gustafsson, and M. Capek, "Capacity bounds and degrees of freedom for MIMO antennas constrained by Q-factor," *IEEE Trans. Antennas Propag.*, vol. 69, no. 9, pp. 5388–5400, 2021.
- [46] K. R. Schab, "Modal analysis of radiation and energy storage mechanisms on conducting scatterers," Ph.D. dissertation, University of Illinois at Urbana-Champaign, 2016.
- [47] M. Gustafsson and M. Capek, "Maximum gain, effective area, and directivity," *IEEE Trans. Antennas Propag.*, vol. 67, no. 8, pp. 5282–5293, 2019.
- [48] M. K. Agoston, *Computer graphics and geometric modeling*. Springer, 2005.